

Rekindling s-Wave Dark Matter Annihilation Below 10 GeV with Breit-Wigner Effects

Geneviève Bélanger,^{1,*} Sreemanti Chakraborti,^{2,†} Cédric Delaunay,^{1,‡} and Margaux Jomain^{1,§}

¹*Laboratoire d'Annecy de Physique Théorique, CNRS – USMB, 74940 Annecy, France*

²*Institute for Particle Physics Phenomenology, Department of Physics Durham University, Durham, DH1 3LE, United Kingdom*

Velocity-independent (s-wave) annihilation of thermal Dark Matter is ruled out by CMB data for masses below ~ 10 GeV, effectively ruling out the possibility of indirectly detecting it in this mass range. We demonstrate in a model-independent framework that Breit-Wigner effects from very narrow resonances can circumvent CMB constraints, thereby reviving the potential to detect s-wave DM annihilation in the present Universe. The density of resonant s-wave Dark Matter continues to evolve long after chemical decoupling, leading to a scenario we refer to as *belated freeze-out*, where kinetic decoupling plays a significant role in determining the relic density.

I. INTRODUCTION

We see the cosmos bright, yet we know it is painted black. The mystery persists: where does dark matter (DM) hide its track? Thermal freeze-out [1–3] remains one of the most compelling mechanisms for producing the DM relic density in the early Universe. However, minimal DM models face strong constraints from a wide range of experimental searches. In particular, weakly interacting DM particles below the electroweak scale are tightly constrained by direct and indirect detection, cosmology, and collider experiments (see *e.g.* [4] for a recent review).

Moreover, since these constraints are governed by DM interactions with the Standard Model (SM), they are often strongly correlated. This correlation can be alleviated if DM annihilation is velocity-dependent. This occurs in p-wave annihilation or even in s-wave when annihilation proceeds via an s-channel resonance. In the latter case, a Breit-Wigner (BW) resonance enhancement at the low DM velocities found in the galactic halo was proposed to explain observed excesses in indirect detection which suggest an annihilation cross-section exceeding the thermal value, $\langle\sigma v\rangle_{\text{th}} \approx 3 \times 10^{-26} \text{cm}^3/\text{s}$ [5–7]. BW enhancement has since been explored as a mechanism for boosting DM annihilation in galaxies in a variety of models [8, 9].

The same effect has been proposed as a way to evade cosmic microwave background (CMB) constraints on GeV-scale DM. Energy injected into the primordial plasma by electrons and photons from DM annihilation affects CMB anisotropies, typically excluding thermal DM for masses below ~ 10 GeV [10]. However, by leveraging the velocity dependence of DM annihilation, these constraints can be avoided (since the DM velocity is very small during the recombination era) while

still allowing sufficient annihilation during freeze-out. This mechanism has been explored for p-wave annihilation [11–13] and is also relevant for s-wave DM annihilation when it occurs near a resonance [13–16]. In contrast to the p-wave and higher-order wave proposals for evading CMB constraints, signals of resonant s-wave DM annihilation are not significantly suppressed and remain potentially observable in the present Universe.

In this work, we take a model-independent approach to s-wave resonant annihilation for DM below the electroweak scale. We determine the allowed parameter space consistent with both relic density and CMB constraints, adjusting the mediator’s mass and width so that the resonance enhancement occurs primarily at the time of DM formation, thus avoiding CMB limits. In particular, we show for various annihilation channels that reproducing the DM relic density while avoiding CMB limits generically requires very narrow resonances with width-to-mass ratio smaller than $\sim 10^{-10}$, depending on DM and mediator masses.

A key feature of resonant annihilation is that DM production extends to much lower temperatures than in standard freeze-out [5]. We highlight that the small couplings typically required to achieve the correct relic density in the presence of a resonance lead to kinetic decoupling of DM during belated freeze-out, significantly impacting DM production [17–19]. To account for this effect, we estimate the decoupling temperature in a model-independent manner and analytically solve the modified Boltzmann equation governing DM number density evolution, assuming dark sector self-interactions are sufficiently rapid for dark states to establish a thermal equilibrium with their own temperature.

We also investigate the impact of DM indirect detection constraints from various astrophysical observations at different distance scales, including XMM-Newton [20] (galactic halo), Fermi-LAT [21] (dwarf galaxies), and MeerKAT [22] (galaxy clusters). We emphasize how current constraints extracted from observations involving different DM velocity regimes depend on the resonance parameters. Our results show that thermal s-wave DM annihilation remains viable below ~ 10 GeV and

* genevieve.belanger@laph.cnrs.fr

† sreemanti.chakraborti@durham.ac.uk

‡ cedric.delaunay@laph.cnrs.fr

§ margaux.jomain@laph.cnrs.fr

presents promising targets for future indirect detection searches, provided the dark sector parameters enable a BW enhancement both during DM formation and in the present Universe. In our model independent approach, we do not discuss direct detection constraints. We expect those to be suppressed due to the small couplings involved [11, 15].

The remainder of this paper is organised as follows. Section II provides a generical discussion of resonant s-wave annihilation, while section III explores its impact on the DM abundance. Section IV summarizes key aspects of kinetic decoupling. Section V presents constraints from CMB anisotropies, and section VI examines current limits from indirect DM searches and presents predictions from BW enhanced s-wave DM annihilation in various. Section VII concludes with a summary of our findings. The appendices include details on the computation of the relic density with and without kinetic decoupling, the average DM velocity after chemical decoupling, and the derivation of CMB bounds.

II. RESONANT S-WAVE ANNIHILATION

Consider a DM particle χ of spin S_χ and mass m_χ , initially in thermal equilibrium with the SM plasma at early times ($T \gg m_\chi$). Near a resonance, its annihilation cross-section takes a generic BW form,

$$\sigma_{\chi\chi \rightarrow f} = \frac{4\pi\omega}{p^2} B_\chi B_f \frac{m_R^2 \Gamma_R^2}{(s - m_R^2)^2 + m_R^2 \Gamma_R^2}, \quad (1)$$

with $\omega \equiv (2J_R + 1)/(2S_\chi + 1)^2$, and $p \equiv \sqrt{s - 4m_\chi^2}/2$ is the DM center-of-mass momentum in terms of the total energy \sqrt{s} . The parameters J_R , m_R , and Γ_R denote the spin, mass, and total width of the resonance, respectively. The branching ratios are given by B_χ for resonance decay into DM pairs and $B_f = 1 - B_\chi$ for other final states. Since the (numerator of the) branching ratios in Eq. (1) are energy-dependent, and assuming s-wave dominance with negligible velocity-suppressed corrections, their product near the resonance follows,

$$B_\chi B_f \simeq \frac{p}{\bar{p}} \bar{B}_\chi \bar{B}_f, \quad (2)$$

where barred quantities denote their ‘‘on-shell’’ values at $\sqrt{s} = m_R$. Introducing the dimensionless parameters $\epsilon_R \equiv m_R^2/(4m_\chi^2) - 1$ and $\gamma_R \equiv m_R \Gamma_R/(4m_\chi^2)$, the annihilation cross-section times the lab-frame DM velocity reads [3],

$$\sigma v_{\text{lab}} = \frac{8\pi b_R (1 + \epsilon)^{1/2}}{m_\chi^2 (1 + 2\epsilon) \epsilon_R^{1/2}} \left[\frac{\gamma_R^2}{\gamma_R^2 + (\epsilon - \epsilon_R)^2} \right], \quad (3)$$

where $\epsilon \equiv (s - 4m_\chi^2)/(4m_\chi^2) \simeq v_{\text{lab}}^2/4$ is the squared relative DM velocity, and we define $b_R \equiv \omega \bar{B}_\chi (1 - \bar{B}_\chi) \leq \omega/4$.

To evade strong CMB constraints while ensuring resonant enhancement at freeze-out, we impose $\epsilon_{\text{CMB}} \ll \epsilon_R \lesssim 1$. When $\epsilon_R \gg \epsilon_{\text{halo}} \sim 10^{-6}$, DM annihilation is only weakly enhanced in the Milky Way, limiting the indirect detection prospects. As we demonstrate below, existing searches already exclude resonant s-wave DM with $\epsilon_R \lesssim 10^{-6}$. We thus focus on ϵ_R in the range $10^{-4} - 10^{-6}$ in the following.

Such a fine-tuned mass coincidence between DM and the mediator is not natural in the ‘t Hooft sense within minimal models. A notable exception arises in Kaluza-Klein DM models [23] based on large extra dimensions [24, 25], where $m_R = 2m_\chi$ can be achieved at tree-level. Nevertheless, this scenario remains phenomenologically compelling, representing one of the last viable scenarios for thermal s-wave DM below $m_\chi \sim 10$ GeV. A key feature of these resonances is their significant impact on freeze-out dynamics, delaying it well beyond the point of chemical decoupling from the thermal bath.

III. BELATED FREEZE-OUT

We assume that DM particles were initially in chemical equilibrium with the SM in the early Universe and that the present relic density of DM has formed through the freeze-out mechanism. The Boltzmann equation governing the number density of DM is given by [1, 26, 27],

$$\dot{n}_\chi + 3Hn_\chi = -\langle\sigma v\rangle(n_\chi^2 - n_{\chi\text{eq}}^2), \quad (4)$$

where H is the Hubble parameter, $n_{\chi\text{eq}}$ denotes the equilibrium DM density, and $\langle\sigma v\rangle$ is the thermally-averaged annihilation cross-section.

Following standard freeze-out calculations for resonant annihilation [3] which are briefly reviewed in appendix A, the contribution of χ to the energy budget of the Universe today is approximately,

$$\Omega_\chi h^2 \simeq 5.5 \times 10^{-13} N_\chi \frac{m_{\chi\text{GeV}}^2 \epsilon_R^{1/2}}{b_R \gamma_R g_\star^{-1/2}}, \quad (5)$$

where $N_\chi = 1$ ($N_\chi = 2$) when χ and $\bar{\chi}$ are (not) identical particles, $m_{\chi\text{GeV}}$ is the DM mass in GeV, and $g_\star^{1/2}$ is the effective number of degree-of-freedom of the SM plasma at the time of chemical decoupling. This expression assumes that DM exchanges energy with the SM sufficiently fast to maintain a thermal distribution throughout freeze-out. However, for highly effective resonant annihilation, this kinetic-equilibrium condition is typically not met [17], as the DM-SM scattering cross-section does not benefit from the resonance and is suppressed by small couplings. In such scenarios, the Boltzmann equation must be solved directly for the DM momentum distribution rather than the number density. This is a challenging numerical task [18], requiring detailed modeling to relate the scattering and annihilation cross-sections. To keep the discussion general, we parameterize corrections

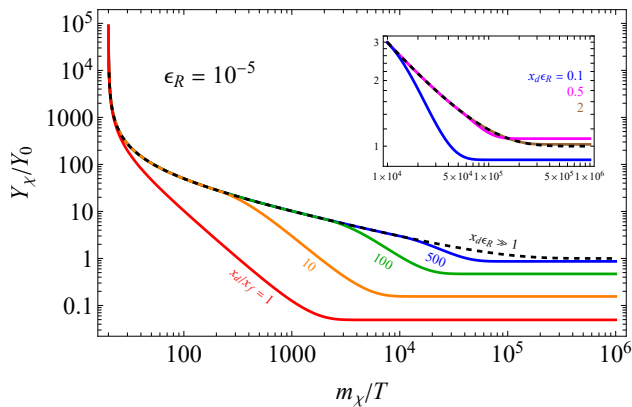


FIG. 1. DM abundance Y_χ as function of time, parameterized by $x = m_\chi/T$, after chemical decoupling at $x_f = 20$ in the belated freeze-out scenario for $\epsilon_R = 10^{-5}$. The dashed line assumes kinetic equilibrium ($x_d \epsilon_R \gg 1$), while the red, orange, green and blue curves represent the suppression due to kinetic decoupling at $x_d/x_f = 1, 10, 100$, and 500 , respectively. The inset highlights the mild enhancement of the abundance for very late decoupling at $x_d \epsilon_R = 1/2$ (magenta) and 2 (brown). Abundances are shown in units of the kinetic equilibrium value at $x \rightarrow \infty$, denoted as Y_0 .

to eq. (5) from early kinetic decoupling with a model-dependent normalization factor k_{dec} . Thus, we write,

$$b_R \gamma_R \epsilon_R^{-1/2} = 4.6 \times 10^{-12} k_{\text{dec}} N_\chi \frac{m_\chi^2 \text{GeV}}{\bar{g}_*^{1/2} f_\chi}, \quad (6)$$

where $f_\chi \equiv \Omega_\chi/\Omega_{\text{DM}}$ is the fraction of the total amount of DM observed, with $\Omega_{\text{DM}} h^2 \approx 0.12$, that is in the form of χ (and eventually $\bar{\chi}$) particles. We will show in section IV that for $\epsilon_R \ll 1$, k_{dec} is expected to be much smaller than unity, meaning the relic density is strongly suppressed, with the approximate scaling $k_{\text{dec}} \propto \sqrt{\epsilon_R}$.

Figure 1 shows that for $\epsilon_R \ll 1$, the abundance of χ continues to evolve long after chemical decoupling, resulting in a belated freeze-out regime. Although the annihilation rate has fallen below the Hubble expansion rate, the annihilation cross-section continues to grow at lower temperatures [5]. As DM particles cool, the peak of their velocity distribution aligns more closely with the resonance peak. Consequently, the DM yield slowly fades out, scaling approximately as $x^{-1/2}$ where $x \equiv m_\chi/T$, until $x \sim \epsilon_R^{-1}$, at which point DM particles are too cold to satisfy the resonance condition. While this description remain qualitatively correct, it is significantly modified by kinetic decoupling, which, as we argue below, likely occurs in the course of this evolution.

IV. KINETIC DECOUPLING

Resonant annihilation typically requires much smaller coupling values to achieve the correct DM relic density. This generally leads to kinetic decoupling of DM during the freeze-out process. Below, we estimate the kinetic-decoupling correction parameter,

$$k_{\text{dec}} \equiv \frac{\Omega_\chi}{\Omega_\chi^{\text{keq}}}, \quad (7)$$

where Ω_χ^{keq} denotes the abundance obtained from eq. (5) under the assumption of kinetic equilibrium.

We assume the DM particles are in sufficiently fast self-interactions, allowing them to form a dark equilibrium at temperature $T' \leq T$ after decoupling at $T = T_d$. For $T \geq T_d$, $T' = T$, while for $T < T_d$, the DM temperature evolves with time according to,

$$T'(T < T_d) \equiv \xi(T)T, \quad \xi(T) = \left[\frac{h_{\text{eff}}(T)}{h_{\text{eff}}(T_d)} \right]^{2/3} \frac{T}{T_d}. \quad (8)$$

The linear scaling with T follows from the fact that DM is non-relativistic at decoupling, while the prefactor captures the subsequent reheating of the SM plasma due to the decoupling of SM species; h_{eff} denotes the number of degrees of freedom of the entropy density.

The right-hand side of the Boltzmann equation in eq. (4) is modified to,

$$\begin{aligned} \dot{n}_\chi + 3Hn_\chi &= -\langle \sigma v \rangle' n_\chi^2 + \langle \sigma v \rangle n_{\chi \text{eq}}^2 \\ &= -\langle \sigma v \rangle [\beta(\xi) n_\chi^2 - n_{\chi \text{eq}}^2], \end{aligned} \quad (9)$$

where $\langle \sigma v \rangle'$ is obtained by taking $T \rightarrow T'$ in $\langle \sigma v \rangle$, and the second line assumes resonant annihilation, with,

$$\beta(\xi) \equiv \xi^{-3/2} e^{-x \epsilon_R (\xi^{-1} - 1)}. \quad (10)$$

We show in appendix B that solving eq. (9) approximately yields,

$$k_{\text{dec}} \simeq \left[\text{erf}(y_d) - \text{erf}(y_f) + \frac{e^{-y_d^2}}{2\sqrt{\pi}y_d} \right]^{-1}, \quad (11)$$

where $y \equiv \sqrt{x \epsilon_R}$, and erf is the error function. The first two terms (last term) in the square brackets correspond to DM annihilation before (after) kinetic decoupling. In the regime $x_d \epsilon_R \ll 1$, the last term dominates, yielding a suppression of the relic density relative to the usual result without kinetic decoupling,

$$k_{\text{dec}} \simeq 2\sqrt{\pi x_d \epsilon_R} \ll 1. \quad (12)$$

Once kinetic decoupling occurs, DM particles, being non-relativistic, cool more rapidly than the thermal bath, with $T' \propto T^2$. This causes the resonance condition to be satisfied earlier, maximizing the annihilation cross-section when the Universe's entropy density is still

high and DM particles are less diluted. As a result, the DM yield decreases more rapidly, scaling approximately as x^{-2} . This effect weakens the later the kinetic decoupling occurs. In the opposite limit, $x_d \epsilon_R \gg 1$, the relic density remains unchanged, as expected, since the DM yield stops evolving after $x \sim \mathcal{O}(\epsilon_R^{-1})$. Interestingly, k_{dec} in eq. (12) reaches a maximum at finite $x_d = (2\epsilon_R)^{-1}$. This implies a window of enhanced relic density, though only by a modest factor of $\mathcal{O}(10\%)$ at most, with a mild ϵ_R -dependence from the $\text{erf}(y_f)$ term. The reason for this is that, at temperatures where the peak of the DM velocity distribution has moved past the resonance, annihilation becomes less efficient. This is because the distribution shifts away from the resonance more rapidly than in kinetic equilibrium, diminishing the overlap of the distribution's tail at later times. When decoupling occurs for $x_d \sim \epsilon_R^{-1}$, where the enhancement discussed earlier has largely diminished, this effect becomes dominant, leading to a slightly higher DM abundance. Figure 1 shows the evolution of Y_χ with time for various kinetic decoupling temperatures.

Kinetic equilibrium is maintained at least until chemical decoupling occurs at $x_f \approx 20$ thanks to the annihilation process itself [11]. Whether kinetic equilibrium persists to lower temperatures depends on the efficiency of scattering processes. While model-dependent, the generic properties of such processes can still be assessed. After chemical decoupling, the scattering rate $n_{\text{SM}} \langle \sigma_{\text{scat.}} v \rangle$ typically remains faster than Hubble expansion because the SM number density n_{SM} is not Boltzmann suppressed, ensuring kinetic equilibrium until well beyond freeze-out in models where the scattering and annihilation cross-sections are comparable. Here, however, unlike annihilation, scattering is not resonantly enhanced and is expected to be suppressed by a factor of $\mathcal{O}(\gamma_R)$ relative to annihilation. For sufficiently small resonance widths, the scattering rate is generically subdominant to the annihilation rate, so kinetic decoupling occurs immediately after chemical decoupling. For larger width values, scattering is less suppressed relative to annihilation, and kinetic decoupling is delayed well after T_f . We show in appendix B that $r_{df} \equiv T_f/T_d$ is, approximately,

$$r_{df} \simeq \begin{cases} \gamma_R/\gamma_R^c & \gamma_R > \gamma_R^c \\ 1 & \gamma_R \leq \gamma_R^c \end{cases}, \quad (13)$$

where $\gamma_R^c \equiv x_f^{3/2} e^{-x_f} \approx 1.8 \times 10^{-7}$. Equation (13) may change in models where additional scattering processes, distinct from the crossing-symmetric counterparts of the annihilation processes, also contribute efficiently to maintain kinetic equilibrium. These processes could extend the period of equilibrium beyond the estimate in eq. (13) and potentially modify the dependence on resonance parameters. In the following, we disregard such processes and assume that eq. (13) remains valid.

V. CMB CONSTRAINTS

DM annihilation during recombination injects energy that heats and reionizes the photon-baryon plasma, affecting the CMB temperature and polarization fluctuations [28]. Observations from the Planck satellite place stringent constraints on DM annihilation at that time [29]. In particular, for annihilation into electron pairs, CMB data exclude cross-sections as large as $\langle \sigma v \rangle_{\text{th}} = 3 \times 10^{-26} \text{ cm}^3/\text{s}$, for DM below $m_\chi \simeq 10 \text{ GeV}$ [10]. This typically rules out standard freeze-out via s-wave annihilation in this channel. However, we show that resonant annihilation can evade these bounds and determine the resonance parameters required for various final states, including electrons, muons, pions, and photons.

At recombination, DM particles are typically very cold, with $\epsilon_{\text{CMB}} \ll 1$ when the Universe's temperature is $T_{\text{CMB}} \approx 2.6 \text{ eV}$. If $\epsilon_R \gg \epsilon_{\text{CMB}}$, the annihilation cross-section at that time is non-resonant and well approximated by the zero-velocity limit ($\epsilon \rightarrow 0$) of eq. (3), typically valid for $\epsilon_R \sim 10^{-5}$ (see appendix C). This gives,

$$\begin{aligned} \langle \sigma v \rangle_{\text{CMB}} &= \frac{8\pi b_R}{m_\chi^2 \epsilon_R^{1/2} (\gamma_R^2 + \epsilon_R^2)} \\ &\approx 2.1 \times 10^{-26} \text{ cm}^3/\text{s} \frac{N_\chi r_{df}^{1/2} \epsilon_R^{1/2}}{\bar{g}_*^{1/2} f_\chi} \left[\frac{\gamma_R}{\gamma_R^2 + \epsilon_R^2} \right], \end{aligned} \quad (14)$$

where we include in the second equality the effect of kinetic decoupling using eq. (12) in eq. (5). The CMB bound can also be evaded if $\epsilon_R \ll \epsilon_{\text{CMB}}$, but since $\epsilon_{\text{CMB}} \lesssim 10^{-11}$ for GeV-scale DM, this would require extreme fine-tuning of dark sector masses, so we do not consider this scenario further.

An upper bound $\langle \sigma v \rangle_{\text{CMB}}$ from CMB anisotropies constrains the resonance width, yielding two possible regimes based on γ_R/ϵ_R (see appendix D): (i) a *large-width* regime with $\gamma_R \gg \epsilon_R$, and (ii) a *small-width* regime with $\gamma_R \ll \epsilon_R$. In the large-width regime, CMB imposes a lower bound on the resonance width,

$$\gamma_R \gtrsim 27 X^2 \left[\frac{\epsilon_R}{10^{-5}} \right], \quad (15)$$

with

$$X \equiv \frac{N_\chi \langle \sigma v \rangle_{\text{th}}}{\bar{g}_*^{1/2} f_\chi \langle \sigma v \rangle_{\text{CMB}}}, \quad (16)$$

which is deeply in the non-perturbative regime unless the CMB bound is significantly weaker than the typical thermal cross section $\langle \sigma v \rangle_{\text{th}}$. Conversely, in the small-width regime, CMB implies a rather strong upper bound on the width,

$$\gamma_R \lesssim \frac{4.5 \times 10^{-8}}{X} \left[\frac{\epsilon_R}{10^{-5}} \right]^{3/2}, \quad (17)$$

provided $\gamma_R < \gamma_R^c$, or

$$\gamma_R \lesssim \frac{7.2 \times 10^{-8}}{X^{2/3}} \left[\frac{\epsilon_R}{10^{-5}} \right], \quad (18)$$

when $\gamma_R > \gamma_R^c$, which suggests very weak resonance's couplings to DM and SM particles in this regime.

Figure 2 shows the allowed resonance widths for DM annihilation into electrons, muons, pions, and photons as a function of the DM mass and for different values of ϵ_R . We use `micrOMEGAs` to derive the CMB constraint for the electron, muon, photon and pion channels, following the approach outlined in [10] and accounting for the most recent Planck data [29]. The pion bound assumes annihilation into both $\pi^0\pi^0$ and $\pi^+\pi^-$ final states, with cross-sections related by isospin symmetry, though the neutral pion contribution largely dominates. Furthermore, for the interested reader, we provide CMB bounds for several individual channels in appendix E.

The small-width regime is bounded from below by the condition $\gamma_R \gtrsim 3.3 \times 10^{-25}/m_\chi \text{GeV}$ that the resonance lifetime does not exceed one second so that it has disappeared from the Universe before the onset of Big Bang nucleosynthesis (BBN), and by the condition $b_R < \omega/4$ corresponding to physically relevant resonance BRs. For electrons with assuming $\epsilon_R = 10^{-5}$, the CMB constraint excludes the large-width regime up to $m_\chi \approx 40$ GeV. In the small-width regime, it forces the resonance to be extremely narrow, as small as $\sim 10^{-12}$ of its mass for $m_\chi \approx 1$ MeV.

For DM below 10 MeV annihilating into electrons and photons, constraints from N_{eff} (not shown in fig. 2) may also be relevant (see, *e.g.*, [30–32]). However, these bounds are model-dependent, as they vary with the DM spin and can be significantly relaxed, in some cases down to $m_\chi \simeq 1$ MeV, if additional couplings to neutrinos are present [30].

VI. INDIRECT DETECTION SIGNALS

We now examine signals of DM annihilation in the present Universe, focusing on the galactic halo, dwarf galaxies, and galactic clusters. For resonant s-wave annihilation, the predicted cross-section depends strongly on the DM velocity. We assume that DM particles have virialized within these astrophysical systems, following a Maxwell-Boltzmann distribution with a dispersion velocity v_{DM} . In the small-width regime, and under the relic density constraint from eq. (6), the velocity-averaged annihilation cross-section is given by,

$$\begin{aligned} \langle \sigma v \rangle &\simeq 1.9 \times 10^{-21} \text{ cm}^3/\text{s} \frac{N_\chi}{\bar{g}_*^{1/2} f_\chi} \left(\frac{v_\odot}{v_{\text{DM}}} \right)^3 \left[\frac{\epsilon_R}{10^{-5}} \right] \\ &\times \exp \left[-18.6 \left(\frac{v_\odot}{v_{\text{DM}}} \right)^2 \left[\frac{\epsilon_R}{10^{-5}} \right] \right], \quad (19) \end{aligned}$$

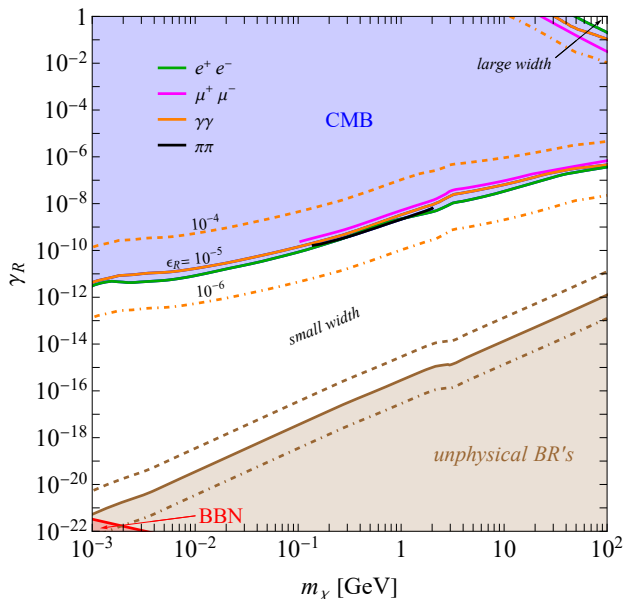


FIG. 2. Resonance width γ_R as function of the DM mass m_χ . The blue-shaded area is excluded by CMB observations with different boundaries representing annihilation to electrons (green), muons (magenta), photons (orange) and pions (black), assuming $\epsilon_R = 10^{-5}$. The pion bound assumes annihilation into both $\pi^0\pi^0$ and $\pi^+\pi^-$ channels, assuming isospin symmetry. The red region corresponds to resonance lifetime exceeding one second, potentially affecting BBN predictions. In the brown-shaded region the resonance branching ratios are not physical ($b_R > \omega/4$, assuming $J_R = 1, S_\chi = 0$). Dashed and dot-dashed lines represent results for resonances with $\epsilon_R = 10^{-4}$ and 10^{-6} , respectively, showing only photons for the CMB exclusion. The allowed regions above and below the CMB exclusion correspond to the large-width and small-width regimes, respectively, as defined in the text.

where $v_\odot \equiv 220$ km/s is the typical velocity dispersion in the Milky Way halo at a distance of ~ 10 kpc from the Galactic center [33, 34]. Notably, $\langle \sigma v \rangle$ in eq. (19) is independent on the resonance width γ_R and only weakly depends on the DM mass via the number of relativistic degrees of freedom present in the early Universe at the time of DM chemical decoupling \bar{g}_* . In astrophysical environments where v_{DM} is much smaller than v_\odot , such as dwarf galaxies, the cross-section is no longer resonantly enhanced and instead approaches the zero-velocity limit,

$$\begin{aligned} \sigma v_0 \equiv \sigma v_{\epsilon \rightarrow 0} &\simeq 6.7 \times 10^{-31} \text{ cm}^3/\text{s} \frac{N_\chi}{\bar{g}_*^{1/2} f_\chi} \\ &\times \left[\frac{\gamma_R}{10^{-12}} \right] \left[\frac{\epsilon_R}{10^{-5}} \right]^{-3/2}, \quad (20) \end{aligned}$$

which is the same cross-section relevant during recombination. Additionally, σv_0 depends weakly on m_χ through \bar{g}_* .

Figure 3 illustrates the boost factor $R \equiv \langle \sigma v \rangle / \sigma v_0$ due to BW effects as a function of the DM dispersion velocity, for different values of ϵ_R and γ_R , highlighting

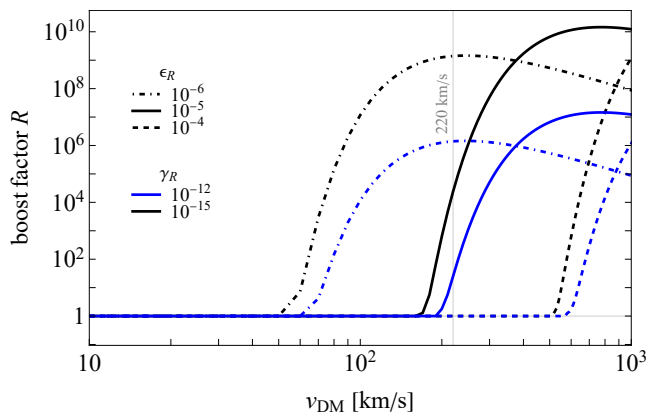


FIG. 3. Boost factor $R \equiv \langle \sigma v \rangle / \sigma v_0$ of the DM annihilation cross-section as function of the DM dispersion velocity v_{DM} , relative to its zero-velocity counterpart, *i.e.*, the cross-section relevant during recombination. Dashed, solid and dot-dashed lines correspond to $\epsilon_R = 10^{-4}$, 10^{-5} and 10^{-6} , respectively, with fixed $\gamma_R = 10^{-12}$ (blue) and 10^{-15} (black). The vertical gray line marks the typical DM velocity dispersion $v_{\odot} = 220$ km/s in the Milky Way’s halo, excluding the Galactic center [33, 34].

the linear dependence of R on γ_R .

A variety of indirect detection (ID) experiments search for the products of DM annihilation in different astrophysical environments. These constraints typically assume a velocity-independent s-wave annihilation cross-section. However, near a resonance, the cross-section exhibits strong velocity dependence, necessitating a recasting of experimental limits.

The Fermi-LAT telescope observes gamma-ray emissions from dwarf galaxies [21], where typical DM velocity dispersions range from 2.5 km/s to 10.7 km/s [35]. At these low velocities, DM annihilation occurs far from the resonance, justifying the zero-velocity approximation $\langle \sigma v \rangle_{\text{Fermi-LAT}} \approx \sigma v_0$. Similarly, for constraints based on gas cooling observations of the Leo T dwarf galaxy [36], where the DM velocity is estimated to be around 7 km/s [37, 38].

Powerful constraints can be extracted from X-ray data of XMM-Newton [20], which observes the entire galaxy and derives limits from concentric rings. We use the constraint from the $42^\circ - 48^\circ$ latitude region, which provides the strongest limits away from the galactic center (GC). In this region, the dominant contribution to DM annihilation comes from DM particles with a velocity v_{\odot} . The X-ray constraints are subject to large uncertainties; here, we adopt the central value from [20].

We also incorporated radio constraints from the MeerKAT telescope, which detects synchrotron emissions from galaxy clusters and dwarf galaxies using radio interferometry [39, 40]. We focus on constraints from galaxy clusters, which have fewer astrophysical uncertainties and provide more robust bounds [22]. Using

DarkMatters [41], we computed the radio flux from DM annihilation into electrons and muons and compared them to MeerKAT’s L-band sensitivity [42]. The typical DM velocity in these clusters is ~ 1000 km/s, resulting in a large boost factor R (see fig. 3) for a wide range of ϵ_R . The constraints in fig. 4 are derived from observations of the Abell 133 cluster [22]. These limits depend on astrophysical parameters, such as the halo radius, density profile, and magnetic field, and can weaken by a factor of 2, or strengthen by over an order of magnitude.

Other constraints from both INTEGRAL [43] and COMPTEL [44] are derived from the inner region of the galaxy, but due to uncertainty in DM velocity in this region, a detailed recasting is required, which we do not perform. Moreover, their limits are generally weaker than those from XMM-Newton, except for DM masses of a few MeV.

Figure 4 presents the predicted annihilation cross-section $\langle \sigma v \rangle_{220} \equiv \langle \sigma v \rangle(v_{\text{DM}} = v_{\odot})$ that satisfies the relic density constraint for different values of ϵ_R , compared to the limits extracted from XMM-Newton ($m_{\chi} < 5$ GeV), Leo T ($m_{\chi} < 1.3$ GeV), Fermi-LAT (for $m_{\chi} > 2$ GeV), and MeerKAT ($m_{\chi} > 5$ GeV), assuming annihilation into e^+e^- (top panel) or $\mu^+\mu^-$ (bottom panel), with $\gamma_R = 10^{-12}$. For $\epsilon_R = 10^{-6}$, the maximum resonant enhancement occurs at v_{\odot} , leading to strong XMM-Newton and MeerKAT constraints that exclude DM over the entire mass range. For $\epsilon_R = 10^{-5}$, XMM-Newton provides the most stringent constraint for $m_{\chi} < 5$ GeV, but does not exclude the relic-density compatible region. Notably, due to resonance effects, very small couplings are required to reproduce the observed DM abundance, leading to $\langle \sigma v \rangle_{220}$ values much smaller than $3 \times 10^{-26} \text{cm}^3/\text{s}$. MeerKAT rules out the region $m_{\chi} > 5$ GeV, as it benefits from a large boost factor. The same conclusion applies to both leptonic channels. For $\epsilon_R = 10^{-4}$, the resonance peak shifts to higher velocities, suppressing $\langle \sigma v \rangle_{220}$ and allowing sub-GeV DM to evade current constraints, while MeerKAT excludes DM in the 5–100 GeV range in both leptonic channels. Due to the small DM velocities involved, dwarf galaxies observations do not benefit from a resonance boost and thus fail to constrain resonant DM for any ϵ_R . Similar conclusions hold for DM annihilation into pion pairs. More precisely, for $\gamma_R = 10^{-12}$, we find that the X-ray constraints are evaded for $\epsilon_R \gtrsim 7 \times 10^{-6}$ for muons and $\epsilon_R \gtrsim 8 \times 10^{-6}$ for electrons, at $m_{\chi} = 1$ GeV, while radio constraints are evaded for $\epsilon_R \gtrsim 2 \times 10^{-4}$ for both electrons and muons at $m_{\chi} = 10$ GeV.

VII. CONCLUSION

In this work, we analyzed the phenomenology of s-wave resonant DM annihilation using a model-independent BW approach. We focused on resonance parameters that significantly enhance DM annihilation during freeze-out,

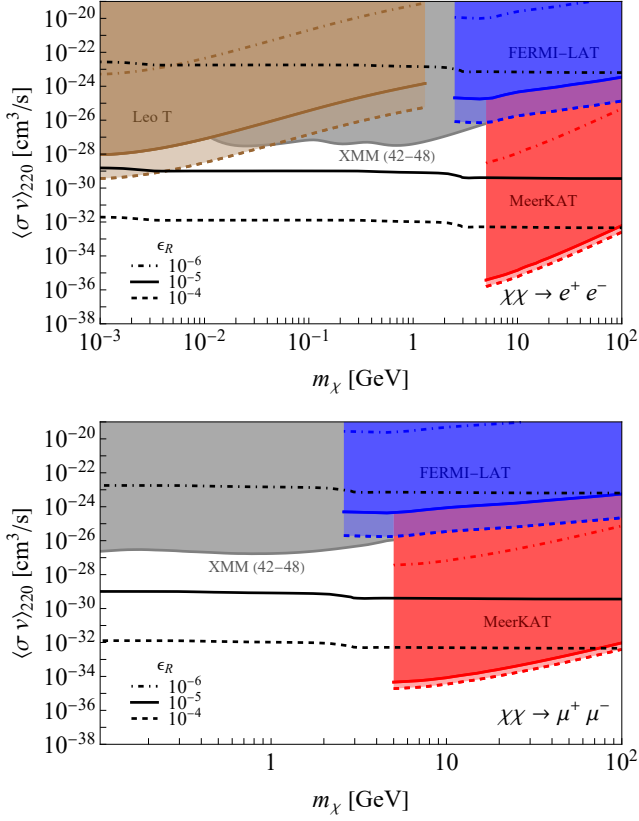


FIG. 4. DM annihilation cross-section $\langle\sigma v\rangle_{220}$ as function of the DM mass m_χ , predicted by the relic density for a typical velocity dispersion $v_\odot = 220$ km/s and $\gamma_R = 10^{-12}$ (black lines). The shaded regions indicate exclusions (recast as described in section VI) from previous DM indirect detection searches in the e^+e^- (top) and $\mu^+\mu^-$ (bottom) channels: Fermi-LAT observations of Milky Way dwarf spheroidal galaxies [21] (blue), constraints from the gas-rich dwarf galaxy Leo T [36] (brown), the galaxy cluster legacy survey by MeerKAT [22] and X-ray observations a latitude ring between 42° and 48° by XMM-Newton [20] (gray). Dashed, solid and dot-dashed lines correspond to $\epsilon_R = 10^{-4}$, 10^{-5} and 10^{-6} , respectively.

allowing for the correct relic density while evading stringent constraints from CMB data. This mechanism revives the thermal s-wave DM scenario for masses below ~ 10 GeV.

The BW effects in DM annihilation enables thermal DM production with much weaker DM-to-SM interactions compared to the standard freeze-out scenario. This leads to early kinetic decoupling during freeze-out and a strong suppression of the relic density. As a result, during recombination, when DM particles are extremely cold, annihilation occurs off-resonance and can be well below the thermal expectation. However, evading current CMB constraints requires the existence of extremely narrow states in the dark sector, with widths in the range $10^{-16} \lesssim \gamma_R \lesssim 10^{-9}$ for $m_\chi = 1$ GeV. This suggests the presence of high-quality approximate dark symmetries.

We also investigated constraints and prospects from indirect detection experiments, which probe DM annihilation across different velocity regimes in the galactic halo, dwarf spheroidal galaxies, and galaxy clusters using data from XMM-Newton, Leo T, Fermi-LAT, and MeerKAT. Among these, XMM-Newton and MeerKAT are particularly effective in further constraining the resonance parameter space, while still leaving room for potential DM annihilation signals in future searches below the electroweak scale. However, future advancements in indirect detection experiments would only improve the sensitivity to the ϵ_R parameter logarithmically.

ACKNOWLEDGMENTS

We thank Alexander Pukhov for his help in improving the spectra tables in `micrOMEGAs` and Geoff Beck for helping with `DarkMatters`. We also thank Marco Cirelli for providing X-ray exclusions for intermediate latitudes. Finally, M. J. thanks Pierre Salati for useful, enthusiastic discussions. S. C. also acknowledges support from the UKRI Future Leader Fellowship ‘‘DARKMAP’’ (Grant No: MR/T042575/1).

Appendix A: Freeze-out near a resonance

We briefly review here the DM relic density’s determination for annihilation near a resonance, following Ref. [3]. The thermal average of the annihilation cross-section times velocity in eq. (3), in the non-relativistic limit and at leading order in $\epsilon_R \ll 1$, yields,

$$\langle\sigma v\rangle = \frac{16\pi^{3/2}b_R\gamma_R}{m_\chi^2}x^{3/2}e^{-x\epsilon_R}, \quad (\text{A1})$$

where $x \equiv m_\chi/T$ and we used the narrow-width approximation, $\gamma_R/[(\epsilon - \epsilon_R)^2 + \gamma_R^2] \rightarrow \pi\delta(\epsilon - \epsilon_R)$ when $\gamma_R \rightarrow 0$. After chemical decoupling at $x = x_f$, n_χ no longer tracks $n_{\chi\text{eq}}$ which becomes negligible in eq. (4). Hence, the DM yield $Y_\chi \equiv n_\chi/s$, with $s = 2\pi^2h_{\text{eff}}(T)T^3/45$ the Universe’s entropy density, solving eq. (4) is approximately [3],

$$Y_\chi^{-1}(x) = Y_f^{-1} + \left(\frac{45}{\pi}G\right)^{-1/2}m_\chi \int_{x_f}^x dx' \frac{g_\star^{1/2}\langle\sigma v\rangle}{x'^2}, \quad (\text{A2})$$

where $G \equiv M_{\text{Pl}}^{-2}$ is Newton’s constant expressed in units of the Planck’s mass $M_{\text{Pl}} \approx 1.2 \times 10^{19}$ GeV,

$$g_\star^{1/2} \equiv \frac{h_{\text{eff}}}{g_{\text{eff}}^{1/2}} \left(1 + \frac{d \log h_{\text{eff}}}{3 d \log T}\right), \quad (\text{A3})$$

and $Y_f \equiv Y_{\chi\text{eq}}(x_f)$. Using eq. (A1) yields,

$$Y_\chi(x) \simeq \frac{3m_\chi\sqrt{5}\epsilon_R^{1/2}}{16\pi^{5/2}M_{\text{Pl}}b_R\gamma_R g_\star^{1/2} \text{erf}(\sqrt{x\epsilon_R})}, \quad (\text{A4})$$

where we neglected the contribution from x_f and the temperature dependence of $g_*^{1/2}$, fixing it instead to $\bar{g}_*^{1/2} \equiv g_*^{1/2}(x_f)$. The relic abundance today is,

$$\Omega_\chi h^2 = 2.8 \times 10^8 \frac{N_\chi m_\chi}{\text{GeV}} Y_\chi(x \rightarrow \infty), \quad (\text{A5})$$

where $N_\chi = 1$ ($N_\chi = 2$) when DM particles and antiparticles are (not) identical. Combining eqs. (A4) and (A5) yields eq. (5) in the main text.

Note that the DM yield evolves long after chemical decoupling, until $x \sim \mathcal{O}(\epsilon_R^{-1}) \gg x_f$, which is in contrast with canonical thermal DM whose yield freezes out soon after x_f . The reason is that $\langle \sigma v \rangle$ in eq. (A1) increases faster at lower temperatures due to the resonance. After chemical decoupling ($x > x_f$), DM particles get colder due to expansion, thus enhancing the probability for two particles to satisfy the resonance condition. In this regime, the DM yield approximately scales as $x^{-1/2}$. Once $x \gtrsim \epsilon_R^{-1}$, particles become too slow to annihilate resonantly and DM freezes out. However, this simple picture is significantly altered by kinetic decoupling which typically occurs beforehand.

Appendix B: Resonant freeze-out with kinetic decoupling

In the presence of kinetic decoupling, assuming $n_\chi \gg n_{\chi \text{ eq}}/\sqrt{\beta}$ after chemical decoupling, the DM yield is still given by eq. (A2) but with the thermal average replaced by $\langle \sigma v \rangle' = \beta \langle \sigma v \rangle$ with β given by eq. (10). Repeating the steps above, we find,

$$Y_\chi(x) = Y_\chi^{\text{keq}}(x) F(\sqrt{x\epsilon_R}), \quad (\text{B1})$$

where Y_χ^{keq} denotes the solution in eq. (A4) obtained assuming kinetic equilibrium. The function $F(y < y_d) = 1$ and,

$$F(y > y_d) \simeq \frac{\text{erf}(y)}{\text{erf}(y_d) + (e^{-y_d^2}/y_d - e^{-y^2}/y)/(2\sqrt{\pi})}. \quad (\text{B2})$$

The χ 's abundance drops faster after kinetic decoupling, scaling approximately as x^{-2} .

Kinetic decoupling occurs when the scattering rate $n_{\text{SM}} \langle \sigma_{\text{scat}} v \rangle$ falls below Hubble expansion, similar to chemical decoupling, which is instead governed by the annihilation rate $n_\chi \langle \sigma v \rangle$. Therefore, in radiation era, the ratio of kinetic to chemical decoupling temperatures $r_{df} \equiv x_d/x_f$ satisfies,

$$r_{df}^2 = \frac{n_\chi \langle \sigma v \rangle}{n_{\text{SM}} \langle \sigma_{\text{scat}} v \rangle}, \quad (\text{B3})$$

where the numerator (denominator) is evaluated at x_f (x_d). Using $n_\chi/n_{\text{SM}} \simeq r_{df}^3 x_f^{3/2} e^{-x_f}$ and assuming that the ratio of scattering to annihilation cross-sections is

typically $\mathcal{O}(\gamma_R)$ due to the resonantly enhanced annihilation yields,

$$r_{df} \sim x_f^{-3/2} e^{x_f} \gamma_R. \quad (\text{B4})$$

For $\gamma_R \lesssim x_f^{3/2} e^{-x_f} \simeq 1.8 \times 10^{-7}$, we have instead $r_{df} \approx 1$ thanks to the efficient energy transfer between DM and SM particles through the annihilation and creation processes.

Appendix C: DM average velocity at recombination

The average velocity of DM after chemical decoupling is,

$$\epsilon(T \leq T_f) = \frac{3T'(T)}{2m_\chi}, \quad (\text{C1})$$

where the DM temperature T' equals the plasma temperature T until kinetic decoupling at T_d after which it evolves as in eq. (8). Kinetic decoupling typically occurs well before recombination, $T_{\text{CMB}} \approx 2.6 \text{ eV} \ll T_d$. Therefore,

$$\epsilon_{\text{CMB}} \equiv \epsilon(T_{\text{CMB}}) = \frac{3T_{\text{CMB}}^2 r_{df}}{2m_\chi^2 x_f}. \quad (\text{C2})$$

Using $x_f = 20$, we obtain $\epsilon_{\text{CMB}} \simeq 2.6 \times 10^{-11} \gamma_R/m_{\chi \text{ GeV}}^2$ for $\gamma_R > \gamma_R^c$, and $\epsilon_{\text{CMB}} \simeq 4.8 \times 10^{-18}/m_{\chi \text{ GeV}}^2$ otherwise. DM is less cold in the former case due to later kinetic decoupling. Restricting to perturbative resonances ($\gamma_R < 1$) then yields an upper limit on DM velocity at recombination,

$$\epsilon_{\text{CMB}} \lesssim 2.6 \times 10^{-11} m_{\chi \text{ GeV}}^{-2}, \quad (\text{C3})$$

which is smaller than 10^{-5} unless $m_\chi \lesssim 2 \text{ MeV}$.

Appendix D: CMB bounds on the resonance width

Combining the CMB and relic density constraints restricts the resonance parameters. The allowed domain in the $b_R - \gamma_R$ plane varies depending on whether $\gamma_R < \gamma_R^c$ or $\gamma_R > \gamma_R^c$. When $\gamma_R < \gamma_R^c$, this yields a quadratic inequality,

$$u_R^2 + 1 - Au_R \geq 0, \quad (\text{D1})$$

where $u_R \equiv \gamma_R/\epsilon_R$ and $A \simeq 0.7X/\sqrt{\epsilon_R}$ with X defined in eq. (16). If the CMB limit is significantly weaker than the thermal cross-section such that $A \leq 2$, the inequality holds for all u_R . In the opposite case, we have $X \gtrsim \mathcal{O}(1)$ and $A \gg 1$ when $\epsilon_R \ll 1$. The inequality is satisfied only outside the two roots,

$$u_R^\pm = \frac{A}{2} \pm \frac{1}{2} \sqrt{A^2 - 4}, \quad (\text{D2})$$

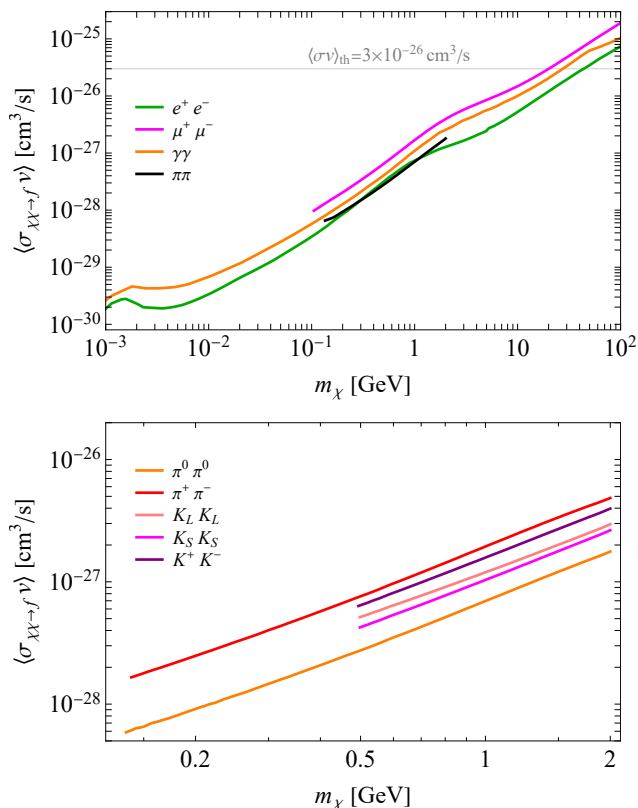


FIG. 5. CMB limits from Planck data for DM annihilation into e^+e^- , $\mu^+\mu^-$, $\gamma\gamma$ and $\pi\pi$ channels (top) and individual hadronic channels (bottom). For the $\pi\pi$ channel we present the limit on the total annihilation cross-section, which includes both the $\pi^0\pi^0$ and $\pi^+\pi^-$ final states, assuming isospin symmetry.

defining two regimes of large and small width. To leading order in large A , these regimes are given by,

$$u_R \gtrsim A, \quad \text{and} \quad u_R \lesssim A^{-1}. \quad (\text{D3})$$

Note that the large width solution is consistent with $\gamma_R < \gamma_R^c$ only when the CMB limit is weaker than the thermal cross-section by four orders of magnitude or more. In practice, it is never consistent for the mass range and annihilation channels under consideration. If instead $\gamma_R > \gamma_R^c$, this results in a fourth-degree inequality,

$$f(u_R) \equiv (u_R^2 + 1)^2 - Bu_R^3 \geq 0, \quad (\text{D4})$$

where $B \simeq 2.7 \times 10^6 X^2$. The number of real positive roots of f is related to its number of turning points. The function f has a local minimum at $x = 0$ with $f(0) = 1$ and $f(x) \simeq x^4 > 0$ for $x \rightarrow \infty$. Moreover, its derivative has two other roots at $x_{\pm} = (3B \pm \sqrt{\Delta})/8$ with $\Delta \equiv 9B^2 - 64$.

Thus, if $B < 8/3$, f has no turning point, and eq. (D4) holds for all u_R . When $B > 8/3$, f turns twice, passing by a maximum at x_- and a second minimum at x_+ . Hence, it has zero or two real positive roots depending on the sign of $f(x_+)$. For $B > 16/(3\sqrt{3}) \approx 3.1$, $f(x_+) < 0$ implying that f has two real positive roots. This defines again two regimes where eq. (D4) holds: one with a large width and another with small one, which, to leading order in large B , are given by,

$$u_R \gtrsim B, \quad \text{and} \quad u_R \lesssim B^{-1/3}. \quad (\text{D5})$$

Note that the small width solution is only consistent with $\gamma_R > \gamma_R^c$ when the CMB limit is weaker than the thermal cross-section by a ~ 4 factor.

Appendix E: CMB limit computation

Our CMB limits are derived with `micrOMEGAs` [45] following the approach of [10, 28] and using the latest Planck constraint [29] on the function

$$P_{\text{ann}} < 3.2 \times 10^{-28} \text{ cm}^3/\text{s}/\text{GeV}, \quad (\text{E1})$$

at 95% confidence level (CL). P_{ann} is related to the annihilation cross-section through the following formula, $P_{\text{ann}} = f_{\text{eff}} \langle \sigma v \rangle / m_\chi$, where

$$f_{\text{eff}} = \frac{\int_0^{m_\chi} E dE \left[2f_{\text{eff}}^{e^+e^-}(E) \left(\frac{dN}{dE} \right)_{e^+} + f_{\text{eff}}^\gamma(E) \left(\frac{dN}{dE} \right)_\gamma \right]}{2m_\chi}, \quad (\text{E2})$$

is the efficiency factor with which the DM rest-mass energy released by annihilation is injected in the intergalactic medium and $(dN/dE)_{e^+,\gamma}$ are the energy spectra of positrons and photons, respectively, produced by the annihilation products. We used `micrOMEGAs` to compute the spectra for electron, muon, photon and scalar mesons, down to sufficiently low energies to derive limits for DM masses as small as 1 MeV. We have verified that the positron and photon spectra are in good agreement with `Hazma` [46, 47] as well as [48] for electron, muon and π^\pm, π^0 annihilation products, for $m_\chi \lesssim 1$ GeV. In addition, we computed the spectra for the K_S, K_L, K^\pm, η and η' scalar mesons and included them in `micrOMEGAs`.

The resulting CMB limits for individual annihilation channels are shown in fig. 5. For $m_\chi \gtrsim 5$ GeV, our limits for the e^+e^- , $\mu^+\mu^-$ and $\gamma\gamma$ channels agree within a few percent with those of [10] derived using `PPPC4DMID` [49], after rescaling the latter by a factor of $3.2/4.1$ to account for the latest Planck constraint. Our limits for the $\pi^0\pi^0$ channel is also in good agreement (below 5%) with [48], while for the $\pi^+\pi^-$ channel our limit is stronger by a factor of 2 near threshold and in good agreement at 1 GeV.

- [1] B. W. Lee and S. Weinberg, *Phys. Rev. Lett.* **39**, 165 (1977).
- [2] M. Srednicki, R. Watkins, and K. A. Olive, *Nucl. Phys. B* **310**, 693 (1988).
- [3] P. Gondolo and G. Gelmini, *Nucl. Phys. B* **360**, 145 (1991).
- [4] M. Cirelli, A. Strumia, and J. Zupan, (2024), [arXiv:2406.01705 \[hep-ph\]](#).
- [5] M. Ibe, H. Murayama, and T. T. Yanagida, *Phys. Rev. D* **79**, 095009 (2009), [arXiv:0812.0072 \[hep-ph\]](#).
- [6] D. Feldman, Z. Liu, and P. Nath, *Phys. Rev. D* **79**, 063509 (2009), [arXiv:0810.5762 \[hep-ph\]](#).
- [7] W.-L. Guo and Y.-L. Wu, *Phys. Rev. D* **79**, 055012 (2009), [arXiv:0901.1450 \[hep-ph\]](#).
- [8] D. Albornoz Vasquez, G. Belanger, and C. Boehm, *Phys. Rev. D* **84**, 095008 (2011), [arXiv:1107.1614 \[hep-ph\]](#).
- [9] Y.-C. Ding, Y.-L. Ku, C.-C. Wei, and Y.-F. Zhou, *Eur. Phys. J. C* **82**, 126 (2022), [arXiv:2110.10388 \[hep-ph\]](#).
- [10] T. R. Slatyer, *Phys. Rev. D* **93**, 023527 (2016), [arXiv:1506.03811 \[hep-ph\]](#).
- [11] G. Bélanger, S. Chakraborti, Y. Génolini, and P. Salati, *Phys. Rev. D* **110**, 023039 (2024), [arXiv:2401.02513 \[hep-ph\]](#).
- [12] Y.-T. Chen, S. Matsumoto, T.-P. Tang, Y.-L. S. Tsai, and L. Wu, *JHEP* **05**, 281 (2024), [arXiv:2403.02721 \[hep-ph\]](#).
- [13] Y.-N. Wang, X.-C. Duan, T.-P. Tang, Z. Wang, and Y.-L. S. Tsai, (2025), [arXiv:2502.18263 \[hep-ph\]](#).
- [14] E. Bernreuther, S. Heeba, and F. Kahlhoefer, *JCAP* **03**, 040 (2021), [arXiv:2010.14522 \[hep-ph\]](#).
- [15] T. Binder, S. Chakraborti, S. Matsumoto, and Y. Watanabe, *JHEP* **01**, 106 (2023), [arXiv:2205.10149 \[hep-ph\]](#).
- [16] S. Balan *et al.*, *JCAP* **01**, 053 (2025), [arXiv:2405.17548 \[hep-ph\]](#).
- [17] T. Binder, T. Bringmann, M. Gustafsson, and A. Hryczuk, *Phys. Rev. D* **96**, 115010 (2017), [Erratum: *Phys.Rev.D* 101, 099901 (2020)], [arXiv:1706.07433 \[astro-ph.CO\]](#).
- [18] T. Binder, T. Bringmann, M. Gustafsson, and A. Hryczuk, *Eur. Phys. J. C* **81**, 577 (2021), [arXiv:2103.01944 \[hep-ph\]](#).
- [19] M. Duch and B. Grzadkowski, *JHEP* **09**, 159 (2017), [arXiv:1705.10777 \[hep-ph\]](#).
- [20] M. Cirelli, N. Fornengo, J. Koechler, E. Pinetti, and B. M. Roach, *JCAP* **07**, 026 (2023), [arXiv:2303.08854 \[hep-ph\]](#).
- [21] M. Ackermann *et al.* (Fermi-LAT), *Phys. Rev. Lett.* **115**, 231301 (2015), [arXiv:1503.02641 \[astro-ph.HE\]](#).
- [22] N. Lavis, M. Sarkis, G. Beck, and K. Knowles, *Phys. Rev. D* **108**, 123536 (2023), [arXiv:2308.08351 \[astro-ph.CO\]](#).
- [23] M. Kakizaki, S. Matsumoto, Y. Sato, and M. Senami, *Phys. Rev. D* **71**, 123522 (2005), [arXiv:hep-ph/0502059](#).
- [24] N. Arkani-Hamed, S. Dimopoulos, and G. R. Dvali, *Phys. Lett. B* **429**, 263 (1998), [arXiv:hep-ph/9803315](#).
- [25] N. Arkani-Hamed, S. Dimopoulos, and G. R. Dvali, *Phys. Rev. D* **59**, 086004 (1999), [arXiv:hep-ph/9807344](#).
- [26] J. Bernstein, L. S. Brown, and G. Feinberg, *Phys. Rev. D* **32**, 3261 (1985).
- [27] R. J. Scherrer and M. S. Turner, *Phys. Rev. D* **33**, 1585 (1986), [Erratum: *Phys.Rev.D* 34, 3263 (1986)].
- [28] T. R. Slatyer, N. Padmanabhan, and D. P. Finkbeiner, *Phys. Rev. D* **80**, 043526 (2009), [arXiv:0906.1197 \[astro-ph.CO\]](#).
- [29] N. Aghanim *et al.* (Planck), *Astron. Astrophys.* **641**, A6 (2020), [Erratum: *Astron.Astrophys.* 652, C4 (2021)], [arXiv:1807.06209 \[astro-ph.CO\]](#).
- [30] N. Sabti, J. Alvey, M. Escudero, M. Fairbairn, and D. Blas, *JCAP* **01**, 004 (2020), [arXiv:1910.01649 \[hep-ph\]](#).
- [31] N. Sabti, J. Alvey, M. Escudero, M. Fairbairn, and D. Blas, *JCAP* **08**, A01 (2021), [arXiv:2107.11232 \[hep-ph\]](#).
- [32] X. Chu, J.-L. Kuo, and J. Pradler, *Phys. Rev. D* **106**, 055022 (2022), [arXiv:2205.05714 \[hep-ph\]](#).
- [33] K. Freese, J. A. Frieman, and A. Gould, *Phys. Rev. D* **37**, 3388 (1988).
- [34] J. W. Moffat, H. Sharron, and V. T. Toth, (2024), [arXiv:2409.17371 \[astro-ph.GA\]](#).
- [35] Y. Zhao, X.-J. Bi, H.-Y. Jia, P.-F. Yin, and F.-R. Zhu, *Physical Review D* **93** (2016), 10.1103/physrevd.93.083513.
- [36] D. Wadekar and Z. Wang, *Phys. Rev. D* **106**, 075007 (2022), [arXiv:2111.08025 \[hep-ph\]](#).
- [37] E. V. Ryan-Weber, A. Begum, T. Oosterloo, S. Pal, M. J. Irwin, V. Belokurov, N. W. Evans, and D. B. Zucker, *Mon. Not. Roy. Astron. Soc.* **384**, 53 (2008), [arXiv:0711.2979 \[astro-ph\]](#).
- [38] E. A. K. Adams and T. A. Oosterloo, *A&A* **612**, A26 (2018), [arXiv:1712.06636 \[astro-ph.GA\]](#).
- [39] K. Knowles *et al.*, *Astron. Astrophys.* **657**, A56 (2022), [arXiv:2111.05673 \[astro-ph.GA\]](#).
- [40] G. Beck and S. Makhathini (2023) [arXiv:2301.07910 \[hep-ph\]](#).
- [41] M. Sarkis and G. Beck, *Phys. Dark Univ.* **47**, 101745 (2025), [arXiv:2408.07053 \[hep-ph\]](#).
- [42] J. Jonas, in *Proceedings of MeerKAT Science: On the Pathway to the SKA — PoS(MeerKAT2016)*, Vol. 277 (2018) p. 001.
- [43] M. Cirelli, N. Fornengo, B. J. Kavanagh, and E. Pinetti, *Phys. Rev. D* **103**, 063022 (2021), [arXiv:2007.11493 \[hep-ph\]](#).
- [44] R. Essig, E. Kuflik, S. D. McDermott, T. Volansky, and K. M. Zurek, *JHEP* **11**, 193 (2013), [arXiv:1309.4091 \[hep-ph\]](#).
- [45] G. Alguero, G. Belanger, F. Boudjema, S. Chakraborti, A. Goudelis, S. Kraml, A. Mjallal, and A. Pukhov, *Comput. Phys. Commun.* **299**, 109133 (2024), [arXiv:2312.14894 \[hep-ph\]](#).
- [46] A. Coogan, L. Morrison, and S. Profumo, *Journal of Cosmology and Astroparticle Physics* **2020**, 056–056 (2020).
- [47] A. Coogan, L. Morrison, T. Plehn, S. Profumo, and P. Reimitz, *JCAP* **11**, 033 (2022), [arXiv:2207.07634 \[hep-ph\]](#).
- [48] A. X. Gonzalez-Morales, S. Profumo, and J. Reynoso-Córdova, *Phys. Rev. D* **96**, 063520 (2017), [arXiv:1705.00777 \[astro-ph.CO\]](#).
- [49] M. Cirelli, G. Corcella, A. Hektor, G. Hutsi, M. Kadastik, P. Panci, M. Raidal, F. Sala, and A. Strumia, *JCAP* **03**, 051 (2011), [Erratum: *JCAP* 10, E01 (2012)], [arXiv:1012.4515 \[hep-ph\]](#).